Electronic Supplementary Information for Predicting allosteric mutants that increase activity of a major antibiotic resistance enzyme

Malgorzata J. Latallo[1,2], George A. Cortina[1,2], Robert K. Nakamoto[1], Salem Faham[1], and Peter M. Kasson[1,2]*

Supplementary Methods:

Enzyme kinetics. Chemicals used are as follows: kanamycin and chloramphenicol were purchased from Fisher Scientific. Nitrocefin was purchased from EMD Millipore (Billerica, MA) and Biovision (Milpitas, CA.) and dissolved in DMSO to form a 10 mM stock solution; any additional dilutions were performed in potassium phosphate saline buffer (pH 7.4). Meropenem sodium carbonate was purchased from LKT laboratories (St. Paul, MN) and used without further purification.

For all kinetic and structural studies, *bla*-CTX-M9 mutants were transformed into the *E.coli* expression strain *BL21-CodonPlus (DE3)-RIPL* (gift of Zygmunt Derewenda). Single-colony stocks were used to inoculate 50 mL LB medium containing 30 mg/mL kanamycin and 34 mg/mL chloramphenicol for overnight growth at 37 °C. 4 ml of each resulting mixture was used to inoculate 2x 500ml TB (Terrific Broth) media containing 30 mg/mL kanamycin and 34 mg/mL chloramphenicol for growth at 37 °C, 220 rpm until OD_{600} measurements reached 1.4. Expression was induced with 0.1 mM isopropyl-b-D-thiogalactopyranoside, and cells were further grown overnight at 18 °C, 220 rpm.

Bacterial cultures were pelleted by centrifugation at 4000 rcf for 20 minutes, the pellets were resuspended in 200 mL ice-cold Sucrose-Tris buffer (pH 9.0) and shaken for 20 minutes at 4 °C. The mixture was centrifuged for 12 minutes at 10500 rcf, 4 °C. Periplasmic protein was then isolated as follows: cell pellets were resuspended in 200 mL 10 mM Tris/HCl pH 9.0, shaken for 20 minutes at 4 °C, centrifuged for 12 minutes at 10500 rcf, 4 °C, and the supernatant containing periplasm was transferred to a fresh tube. Periplasmic protein was precipitated with ammonium sulfate and resuspended in TEAA buffer (pH 7.4). After overnight dialysis, protein purified via anion exchange chromatography (HiTrap Q FF, GE Healthcare, Sweden), followed by size exclusion chromatography (Superdex 75 10/300 GL, GE Healthcare, Sweden). Eluted protein was dialyzed in 100mM PBS buffer pH 7.4 at 4 °C. The protein concentration was estimated using both 260/280 nm absorbance ratios and BCA assays. Enzymatic purity was assessed by SDS-PAGE.

Steady-state hydrolysis kinetics were measured as follows: nitrocefin was mixed with CTX-M9 enzyme or the indicated mutant in 10mM PBS, pH 7.4 to a final concentration of 0.2 nM enzyme and 2-200 μM nitrocefin as indicated. Nitrocefin hydrolysis was measured using absorbance at 486 nm at 15 s intervals using a Spectramax reader (Molecular Devices, Sunnyvale, CA). Initial velocities were determined by linear fits to the first portion of each reaction, and K_M and k_{cat} values were determined by nonlinear fits of initial velocities as a function of substrate concentration. A change in absorbance at 486-490 nm indicates formation of the acyl intermediate or any later stage in nitrocefin hydrolysis and thus reports on [EI] + [EP] + [P]. Fits of initial velocity data to estimate K_M and k_{cat} incorporated data from at least two biological replicas per mutant per concentration.

Thermostability assays. Protein melting temperatures were measured using a SYPRO orange thermostability assay (Life Technologies, Carlsbad, CA). Dye fluorescence was monitored continuously in a real time PCR machine (Bio-Rad, Hercules, CA). All measurements were carried out in 10 mM phosphate buffer saline (pH 7.4) with 40 μM protein for *apo* enzyme. The meropenem adduct with CTX-M9 was formed by mixing an enzyme to a final solution of 40 μM with 200 μM meropenem (aqueous stock solution). Enzyme-adduct mixture was incubated on ice for 10 minutes prior to measurement. All meas-

urement runs were performed in 0.5°C increments from 20°C to 90°C. Melting temperatures were determined as the greatest magnitude of the derivative of the observed fluorescence.

Structural studies. Crystals of CTX-M enzymes mutants were grown by vapor diffusion using sitting drops at 21 °C over buffer. CTX-M9-T165W was crystallized by mixing an equilibration mixture of 0.7 M potassium phosphate, 18% PEG 3350, pH of 8.2 1μl with 1μl of enzyme at 5 mg/mL in 10 mM sodium phosphate pH 7.5 Crystals were harvested after 7 days. CTX-M9 L48A was crystallized by mixing 1.2 M potassium phosphate pH 8.2 1μl with 1μl of enzyme at 20 mg/ml in 10 mM sodium phosphate pH 7.5. Crystals were harvested after 30 days. CTX-M9 S281A was crystallized by mixing 0.6 M sodium phosphate buffer, 20% PEG 3350, pH 8.4 with 1μl of enzyme (24 mg/mL in 10 mM sodium phosphate pH 7.5). Crystals were harvested after 90 days and diffracted to 6 Å. Crystals were flash frozen in liquid nitrogen prior to data collection.

Data were collected at beamlines 22-ID (T165W) and 22-BM (L48A) at the Advanced Photon Source at 100 K. Reflections were indexed, integrated and scaled using X-ray Detector Software (XDS) for T165W and the HKL software package for L48A, followed by further processing with CCP4 [1]. Structures were solved by molecular replacement using Phaser [2] with chain A of the native CTX-M9 crystal as the starting model (PDB ID: 1YLJ). Rebuilding was performed in Coot [3] followed by refinement with isotropic B-factors using Refmac. Water, PEG, chloride and phosphate molecules were added manually by examination of the Fo-Fc and 2Fo-Fc electron density maps.

Simulation preparation and equilibration. The acylated meropenem and cefotaxime structures of CTX-M9 wild-type were generated using rigid-body fitting as previously described[4] using the native CTX-M9 crystal structure 1YLJ[5] as a starting model. Point mutations were modeled using MODELLER's automodel[6] method. Histidine tautomer choices were determined automatically by the GROMACS[7] pdb2gmx utility; active-site protonation states were determined using PROPKA[8], with the remainder automatically determined by GROMACS pdb2gmx. The protein was placed in an octahedral box with a minimum of 2nm separation between periodic images and energy-minimized for 500 steps of steepest-descent minimization in vacuum. The protein was then solvated with TIP3P water and 150 mM NaCl; deacylating waters were not placed manually but spontaneously took the appropriate position during simulation. After solvation, another 500 steps of energy minimization were performed followed by 50,000 steps of NVT equilibration with 2 fs timesteps prior to production simulation with identical settings but in an NPT ensemble using the velocity-rescaling thermostat[9] and Berendsen barostat. Velocities were randomly sampled at start from a Maxwell distribution. Pressure coupling was performed at 1 bar with a 10 ps relaxation constant and a compressibility of 10^{-4} bar^{-1}. Temperature coupling was performed at 37 ºC with a time constant of 10 ps. A direct-space cutoff of 1.2 nm was used for both van der Waals and electrostatic interactions, and long-range electrostatics were treated using Particle Mesh Ewald[10] with a grid spacing of 0.15 nm. Hydrogen bonds were constrained using LINCS[11].

Sequence analyses. CTX-M family enzyme sequences were retrieved using previously curated accession numbers[12]. A second, broader sequence alignment was generated using the 500 sequences most closely related to CTX-M9 using a PHMMER search[13], discarding one that had a >50% length mismatch. Amino acid multiple sequence alignments were generated using MUSCLE[14]. Phylogenetically corrected sequence mutual information (MI_p) was computed using the APC correction detailed previously[15].

Rigidity analyses. The KINARI software[16] was used to predict rigid clusters based on the crystal struc-tures of wild-type CTX-M9 (2P74), L48A (5KMT), and T165W (5KMU) at 11 evenly-spaced cutoffs for hydrogen bonds and hydrophobic interactions, determined based on the highest and lowest interaction energies calculated by KINARI in the wild-type crystal structure. Each atom-atom interaction was as-signed a rigidity score consisting of the number of rigid clusters in which the pair co-existed across all 11 cut-off levels. Residue-residue scores were computed as the sum of all component atom-atom rigidity scores, and the per-row maximum of resulting matrix was calculated to yield residues most strongly par-ticipating in rigid-body interactions for each crystal structure. A complementary analysis was performed using MSU ProFlex[17]: 11 evenly spaced energy cutoffs were again used, and the most stringent cutoff before breakup of the large rigid core was selected. To test the effect of side-chain interactions on the stability of this core, each non-Ala residue in CTX-M9 was computationally mutated to alanine using MODELLER[6], rigid cluster analysis was performed on the resulting set of mutant structures, and each residue was scored based on similarity between the predicted rigid cluster for its alanine point mutant and the wild-type structure.

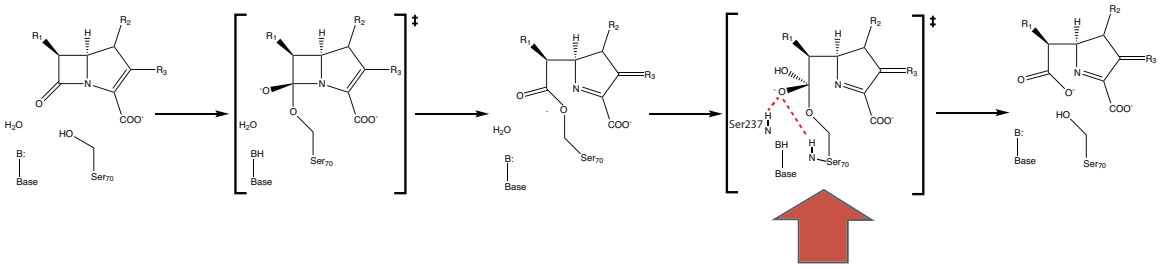

Figure S1. Schematic of deacylation intermediates and hydrogen bond stabilization. A schematic of β-lactam hydrolysis is given, with a red arrow denoting the deacylation tetrahedral intermediate. The oxyanion in this state is stabilized by hydrogen bonds to backbone amide protons on residues 237 and 70 (dotted red lines) as well as an intramolecular hydrogen bond on the β-lactam. Mutations were scored based on the probability of satisfying both of these hydrogen bonds in the acyl intermediate state, using a 3 Å distance criterion for hydrogen bonding, across all simulation snapshots, which were recorded at 50 ps intervals. It is hypothesized that the presence of these hydrogen bonds should reduce the activation free energy barrier for deacylation.

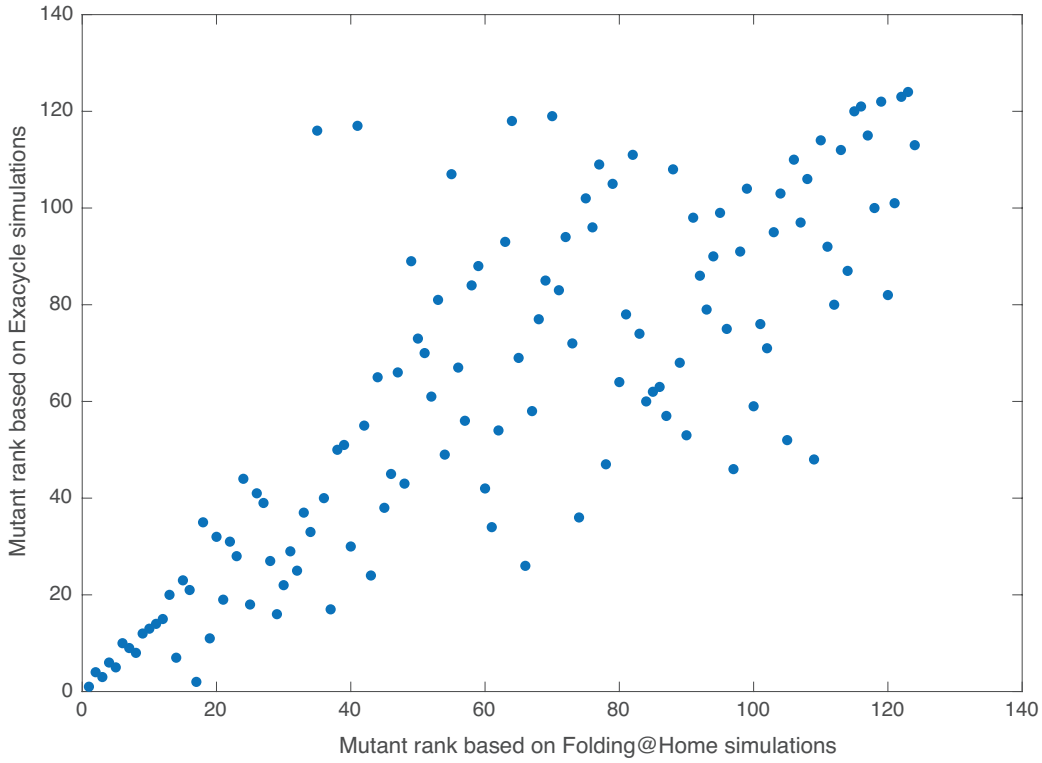

Figure S2. Comparison of mutant scoring from two simulation data sets. CTX-M9 point mutants were scored based on predicted oxyanion hole probability in one of two simulation datasets, the 50 longest simulations computed using Folding@Home and the 1000 shorter simulations computed using Google Exacycle. The rankings were not significantly different (p=0.885 via Wilcoxon Rank Sum Test), and the concordance was particularly strong among high-ranking mutants (lower left corner of plot).

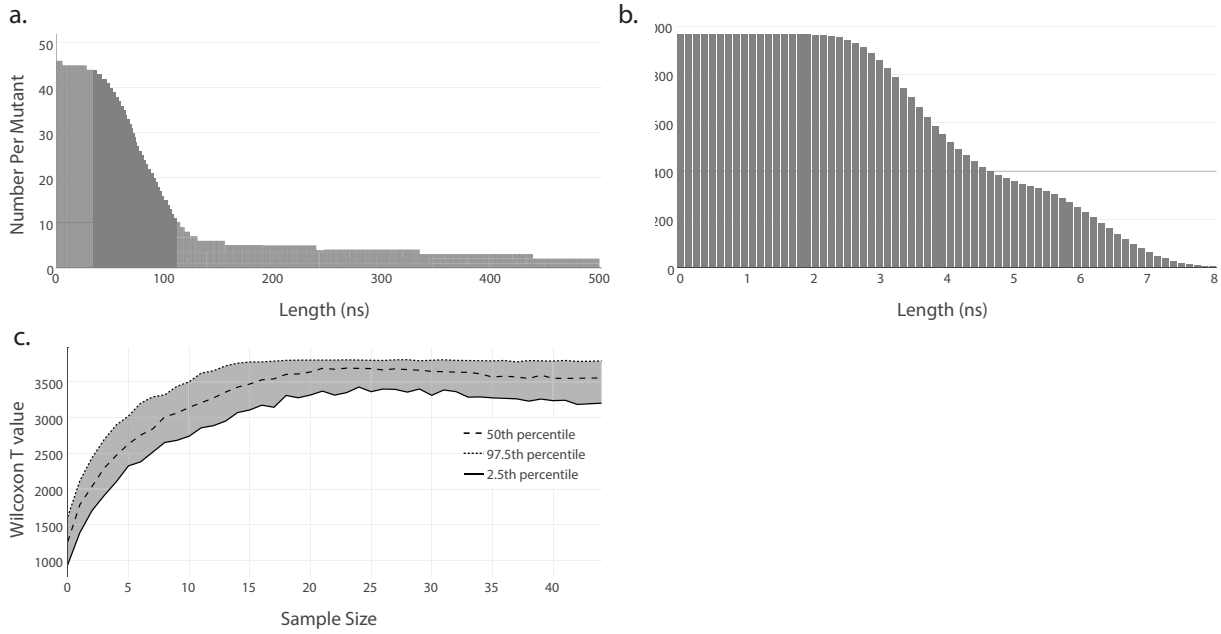

Figure S3. Lengths of simulations per dataset and convergence of mutant ranking. Plotted in panels **a** and **b** are cumulative distribution functions of the average simulation length per mutant in the Folding@Home dataset and the Exacycle dataset. The first 500 ps of each Exacycle trajectory and the first 5 nanoseconds of each Folding@Home trajectory were excluded from oxyanion hole analysis. Plotted in panel **c** is a convergence analysis using the Folding@Home trajectory data. Trajectories were bootstrap-resampled from the original dataset, oxyanion hole scores calculated, and then a Wilcoxon Rank Sum test was performed between the ranking of mutants on the full dataset and the ranking of mutants on each resampled dataset. Convergence of the rankings was achieved at approximately 25 simulation trajectories per mutant (averaging 57.5 ns each).

Mutant	Cefotaxime Oxyanion Hole Score	90% Confidence Interval (20 sims)
T165W	0.99991	(0.9993, 1.0)
S281A	0.999	(0.997, 1.0)
L48A	0.984	(0.963, 1.0)
WT	0.973	(0.943, 1.0)
Mutant	**Meropenem Oxyanion Hole Score**	**Standard Deviation (1000 sims)**
T165W	0.58	0.005
A140K	0.55	0.021
T266R	0.51	0.002
S281A	0.48	0.002
L48A	0.48	0.001
N271D	0.46	0.006
S220R	0.45	0.006
P167L	0.44	0.006
H112Y	0.42	0.006
N106S	0.4	0.007
Q254T	0.33	0.009
T71S	0.31	0.011
T202P	0.3	0.008
A219H	0.3	0.017
K137L	0.26	0.01
T168E	0.24	0.01
D277A	0.21	0.01
E158T	0.2	0.009
A35K	0.17	0.008
S274H	0.17	0.008
Q93T	0.16	0.008
Q141E	0.15	0.01
A100N	0.14	0.013
Q89G	0.13	0.009
M186V	0.11	0.008
V95I	0.1	0.008
M68L	0.08	0.008
I247Y	0.08	0.008
A47Y	0.07	0.007
S39D	0.07	0.006
Q267A	0.07	0.008
G115T	0.07	0.008
L225V	0.07	0.008
N104P	0.06	0.007
S72P	0.05	0.007
Y105W	0.05	0.006
V113L	0.05	0.006
I49M	0.04	0.006
Q192K	0.04	0.006
G62A	0.03	0.005

T244A	0.03	0.011
D101A	0.03	0.005
A287L	0.02	0.005
A52G	0.02	0.004
D53S	0.02	0.005
A218N	0.02	0.005
A231V	0.02	0.006
A187T	0.02	0.004
S27-	0.02	0.003
M135A	0.01	0.002
E96R	0.01	0.001
N114T	0.01	0.003
R275S	0.01	0.004
I285L	0.01	0.003
M75F	0.01	0.003
T209D	0.01	0.005
A76L	0.01	0.006
I139L	0.01	0.004
S40F	0.01	0.004
-238C	0.01	0.004
Q83R	0.01	0.003
Q56T	0.01	0.004
D63E	0.01	0.003
D240V	0.01	0.003
E201A	0.01	0.001
H197S	0.01	0.007
T116G	0.0	0.001
L119V	0.0	0.002
T171S	0.0	0.0
L127V	0.0	0.001
T133A	0.0	0.001
N92D	0.0	0.0
K88A	0.0	0.004
T86Q	0.0	0.0
V148L	0.0	0.002
A152M	0.0	0.001
E85Q	0.0	0.001
K82A	0.0	0.001
V74G	0.0	0.0
P177A	0.0	0.001
T181S	0.0	0.002
T182S	0.0	0.001
K98G	0.0	0.001
Q188E	0.0	0.003
T189S	0.0	0.003
R191Q	0.0	0.002
G200A	0.0	0.001
L59S	0.0	0.002
A205Q	0.0	0.002
L207F	0.0	0.002

A109S	0.0	0.0
T55A	0.0	0.001
I97Y	0.0	0.001
L33F	0.0	0.002
N54G	0.0	0.0
I250V	0.0	0.002
Q31-	0.0	0.004
V29-	0.0	0.001
S228D	0.0	0.0
T230A	0.0	0.001
I286A	0.0	0.001
S237T	0.0	0.003
L44I	0.0	0.0
A28-	0.0	0.0
R43S	0.0	0.003
L279I	0.0	0.002
R276E	0.0	0.001
W273K	0.0	0.001
G224A	0.0	0.0
L259I	0.0	0.001
V262A	0.0	0.0
T263V	0.0	0.001
F265T	0.0	0.001
K38Q	0.0	0.001
T227A	0.0	0.004
Q269N	0.0	0.001
Q270K	0.0	0.001
K32P	0.0	0.0
A272D	0.0	0.0
P99K	0.0	0.001
T26-	0.0	0.0
WT	0.01	0.006

Table S1. Listing of oxyanion hole scores computed for acylenzyme complexes with meropenem for all 125 CTX-M9 mutants and for cefotaxime with 3 CTX-M9 mutants. Uncertainties were calculated via bootstrap resampling across trajectories. For 1000-trajectory meropenem datasets, a normal approximation held and standard deviations are reported, while for 20-trajectory cefotaxime datasets, 90% confidence intervals are reported. The 20-simulation cefotaxime dataset is somewhat undersampled, likely because the oxyanion-hole to non-oxyanion-hole transition rate is slower than for meropenem. Nonetheless, the oxyanion hole rank ordering is preserved between the two sets of simulations. Deletions are denoted by a mutation to - and insertions by a mutation from -.

Rank	Mutant	Score
1	T266R	0.84
2	S281A	0.84
3	T165W	0.81
4	H112Y	0.75
5	N106S	0.75
6	N271D	0.70
7	S220R	0.69
8	L48A	0.67
9	Q254T	0.62
10	P167L	0.58
Mutants scored by angle between the two oxyanion-stabilizing H-bonds:		
1	S281A	0.57
2	T266R	0.53
3	H112Y	0.52
4	T165W	0.52
5	L48A	0.49
6	Q254T	0.48
7	N271D	0.46
8	S220R	0.46
9	N106S	0.44
10	K137L	0.43

Table S2. Top-scoring mutations via alternate hydrogen-bond scoring metrics. Listed above are the top ten mutations scored via hydrogen-bond angle as well as distance criteria using simulations of the meropenem acylenzyme. Listed below are the top ten mutations scored by the angle between the two oxyanion-hole-stabilizing hydrogen bonds. Here, simulations were scored by what fraction of snapshots had an angle of 109.5º +/- 10º, corresponding to the geometry of a tetrahedral oxyanion intermediate. Using hydrogen-bond angle criteria, 9 of the top 10 mutants are identical although ordered differently; using the angle between the hydrogen bonds, 8 of the top 10 are identical and our three experimentally validated mutants still rank in the top five.

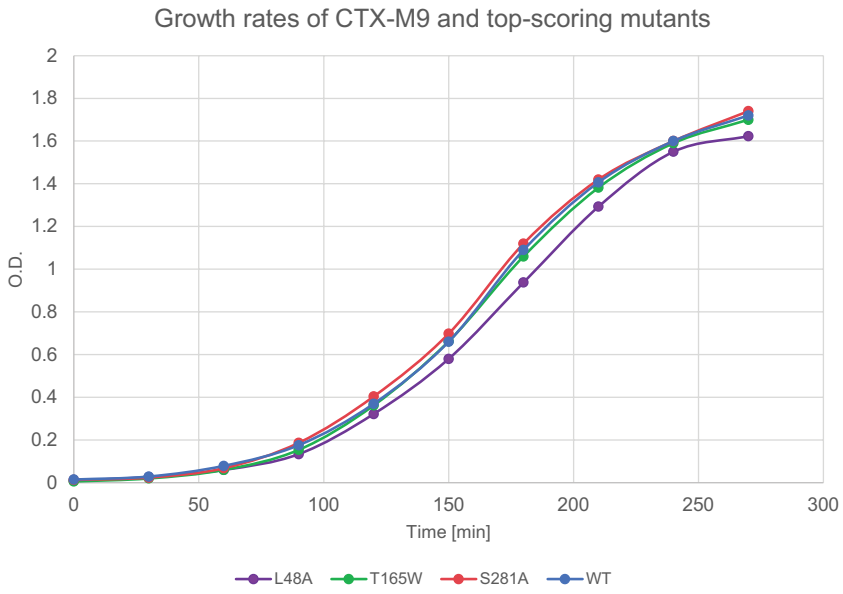

Figure S4. Growth rates of bacteria expressing CTX-M9 and top-scoring drug resistance mutants are nearly indistinguishable. Optical density is plotted as a function of time for identically inoculated samples from log-phase cultures in LB broth. Wild-type CTX-M9, T165W, and S281A overlay precisely, while L48A displays a very mild growth delay.

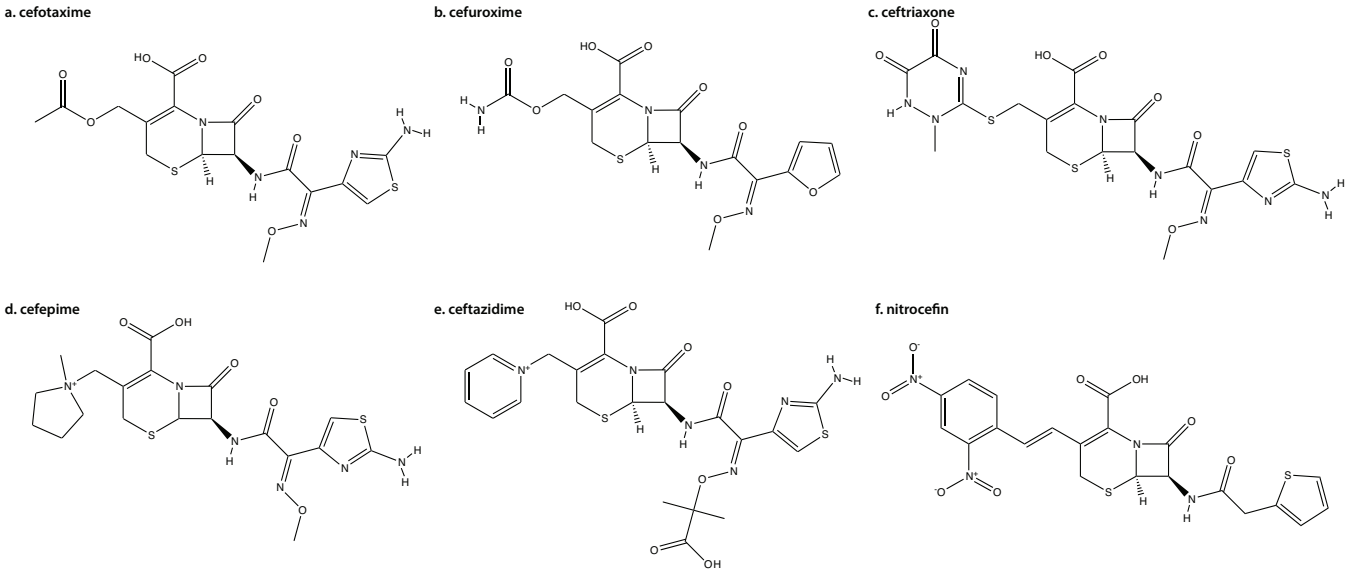

Figure S5. Chemical structures for cephalosporin drugs used.

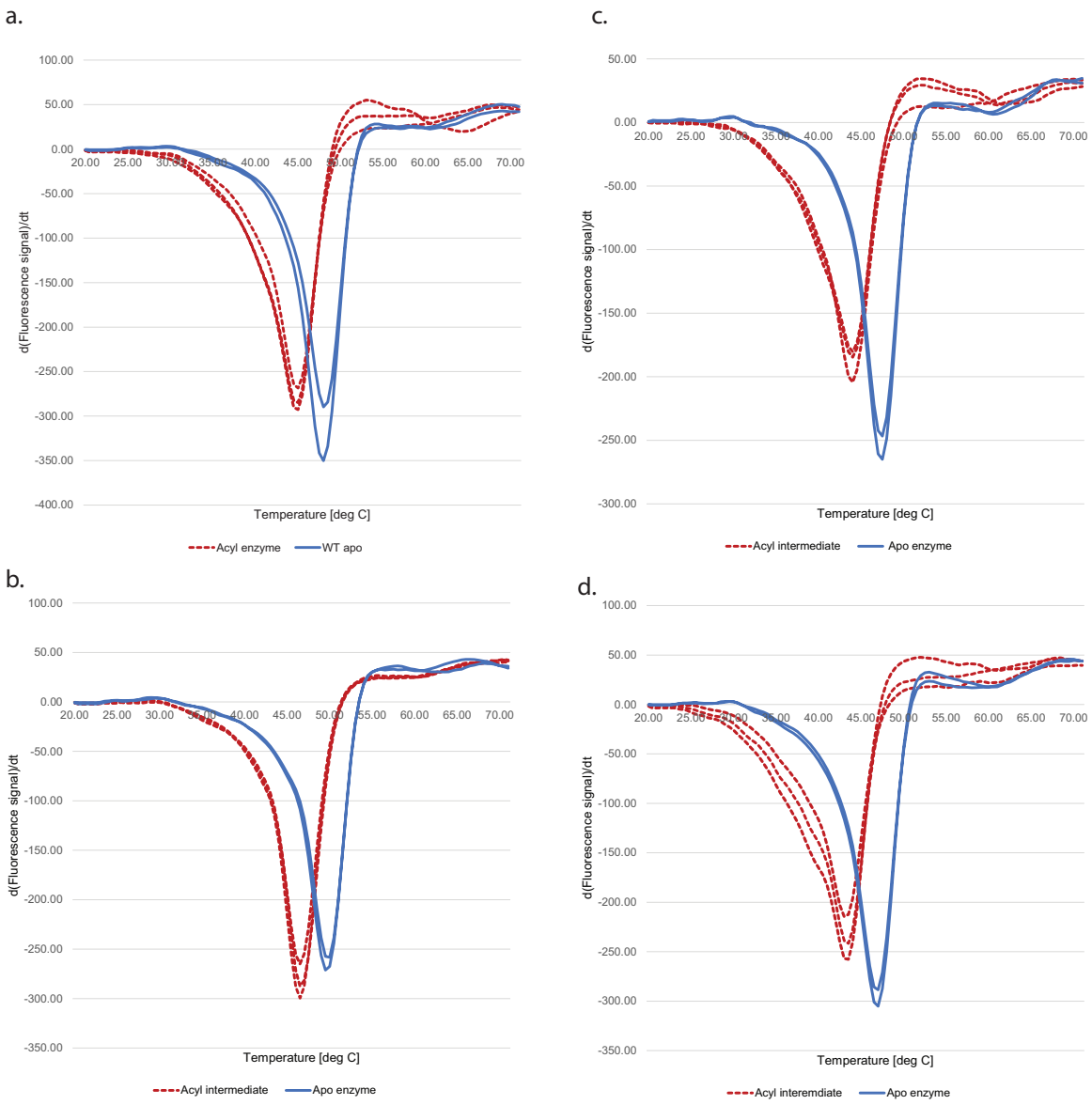

Figure S6. Thermal melting curves of CTX-M9 and top mutants in apo- and acylenzyme forms. Derivatives of hydrophobic dye fluorescence with respect to temperature are plotted for CTX-M9 (**a**), L48A (**b**), T165W (**c**), and S281A (**d**). Apo enzymes were run in duplicate and meropenem-acylenzyme conjugates in triplicate; all runs were highly reproducible and sharply peaked.

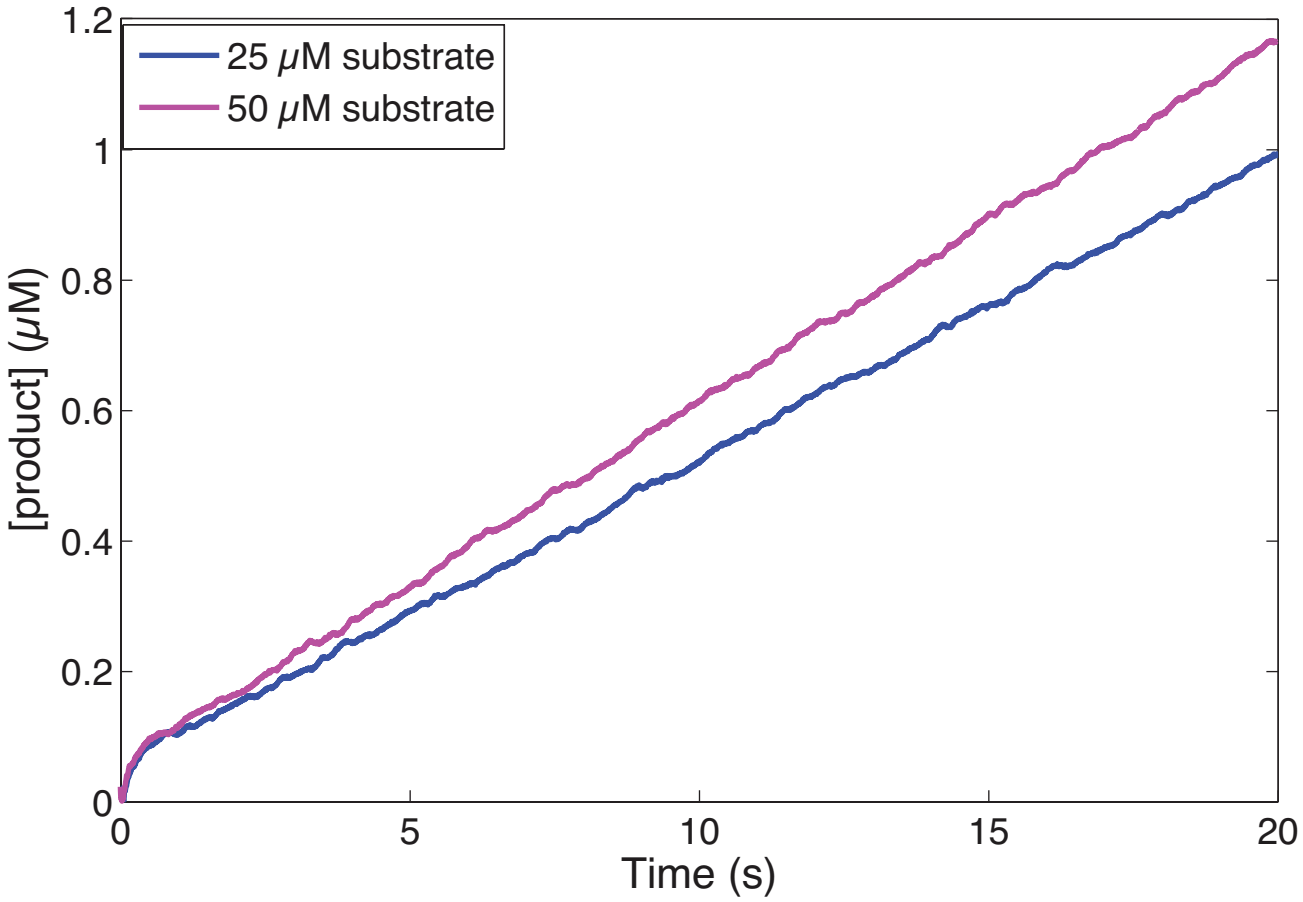

Figure S7. Pre-steady-state kinetics of CTX-M9 show that acylation is not rate-limiting for nitrocefin hydrolysis. Hydrolysis of nitrocefin was initiated using a stopped-flow mixer and monitored via UV absorption at 486 nm, which is characteristic of acylenzyme intermediate and/or hydrolyzed product. This acylation product showed a burst phase of amplitude ~80 nM prior to steady-state reaction progress for an enzyme concentration of 0.5 nM. Such a burst phase indicates that acylation is not rate-limiting for nitrocefin hydrolysis; a non-stoichiometric burst phase has been previously analyzed for other beta lactamases and is characteristic of either a branching reaction pathway for deacylation or an off-pathway intermediate in the acylenzyme state[18, 19]. Enzyme kinetics were measured at 278 ºK, 0.5 nM enzyme, and either 25 μM or 50 μM nitrocefin as indicated.

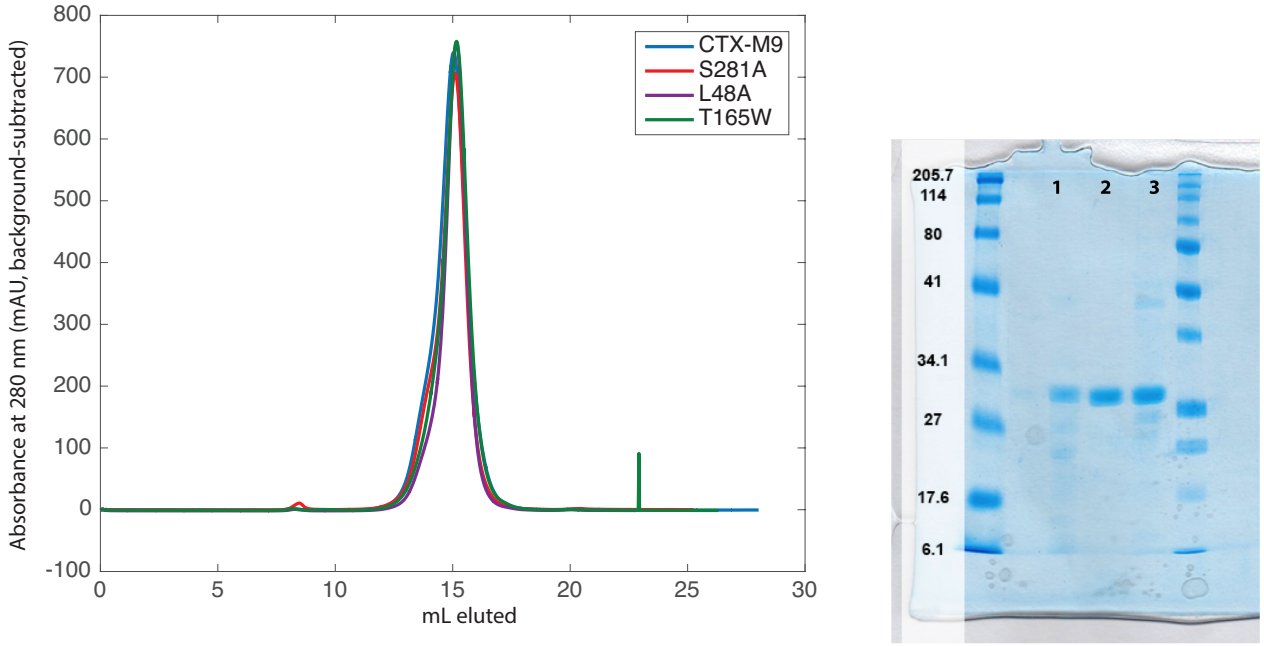

Figure S8. Final column elution profiles from CTX-M9 and top mutants and SDS gel of mutants. Integrated and background-subtracted absorbance values normalized to 1.5 L of culture grown and treated identically reflect the amount of expressed, folded protein and were 39.2 AU for CTX-M9, 38.0 AU for L48A, 37.7 AU for T165W, and 38.6 AU for S281A. A photograph of an SDS-page gel of the column eluant for each of the mutants is shown at right with CTX-M9 L48A in the lane marked 1, T165W in 2, and S281A in 3.

	CTX-M9 L48A	CTX-M9 T165W
Data collection		
Space group	$P3_2$	$P2_1$
Cell dimensions		
a, *b*, *c* (Å)	41.79, 41.79, 232.40	42.74, 42.21, 68.03
a, *b*, *g* (°)	90.00, 90.00, 120.00	90.0, 104.52, 90.0
Resolution (Å)	50.00-1.70 (1.73-1.70)	32.93-1.80 (1.84-1.80)
R_{merge}	7.4 (30.5)	6.7 (38)
I/sI	26.8 (5.9)	17.4 (3.6)
Completeness (%)	94.8 (66.1)	95.52 (70.30)
Redundancy	8.1(4.6)	6.7 (4.3)
No. reflections collected	382397/47330	140968/20959
Refinement	REFMAC 5.7	REFMAC 5.7
Resolution (Å)	1.70	1.80
No. reflections	45006	19869
R_{work}/ R_{free}	0.19/0.22 (0.22/0.26)	0.16/0.18 (0.21/0.28)
No. atoms		
Protein	1937, 1938	1980
Ligand/ion	24	42
Water	448	137
B-factors		
Protein	22.05, 21.95	18.78
Ligand/ion	35.48	54.27
Water	25.44	27.54
R.m.s deviations		
Bond lengths (Å)	0.024	0.025
Bond angles (°)	2.365	2.396

Structure solved based on reflection data from a single crystal. Numbers in parentheses are for the highest resolution shell.

Table S3. Crystallographic statistics for structures of CTX-M9 L48A and T165W.

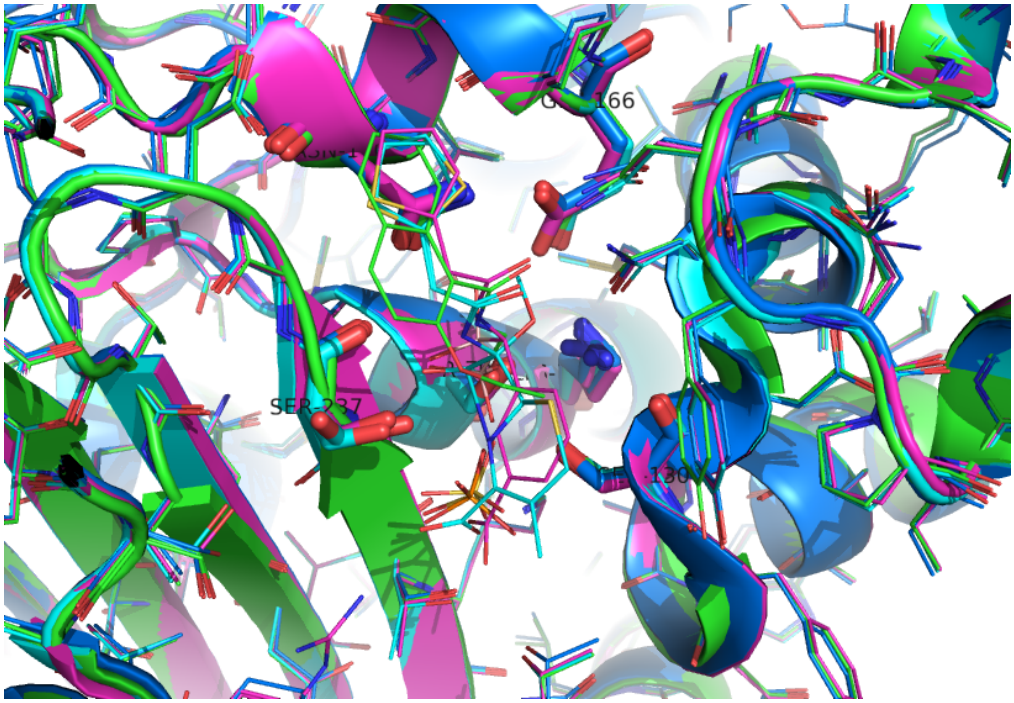

Figure S9. Minimal movement of catalytic side-chains in previously determined crystal structures of CTX-M9 throughout the catalytic cycle. Rendered is an overlay of previously reported crystal structures for CTX-M9 apoenzyme (blue), and in complex with an acylation transition state analogue (green), acylated to cefoxitin (cyan), and in complex with a deacylation transition state analogue (pink). Active site residues, including catalytic residues, undergo only very subtle conformational changes between these structures. Heavy-atom RMSD of active-site residues are 0.19 Å, 0.32 Å, and 0.30 Å respectively. Structures rendered correspond to PDB IDs 1YLJ[5], 1YMX, 1YMS, and 1YM1[20].

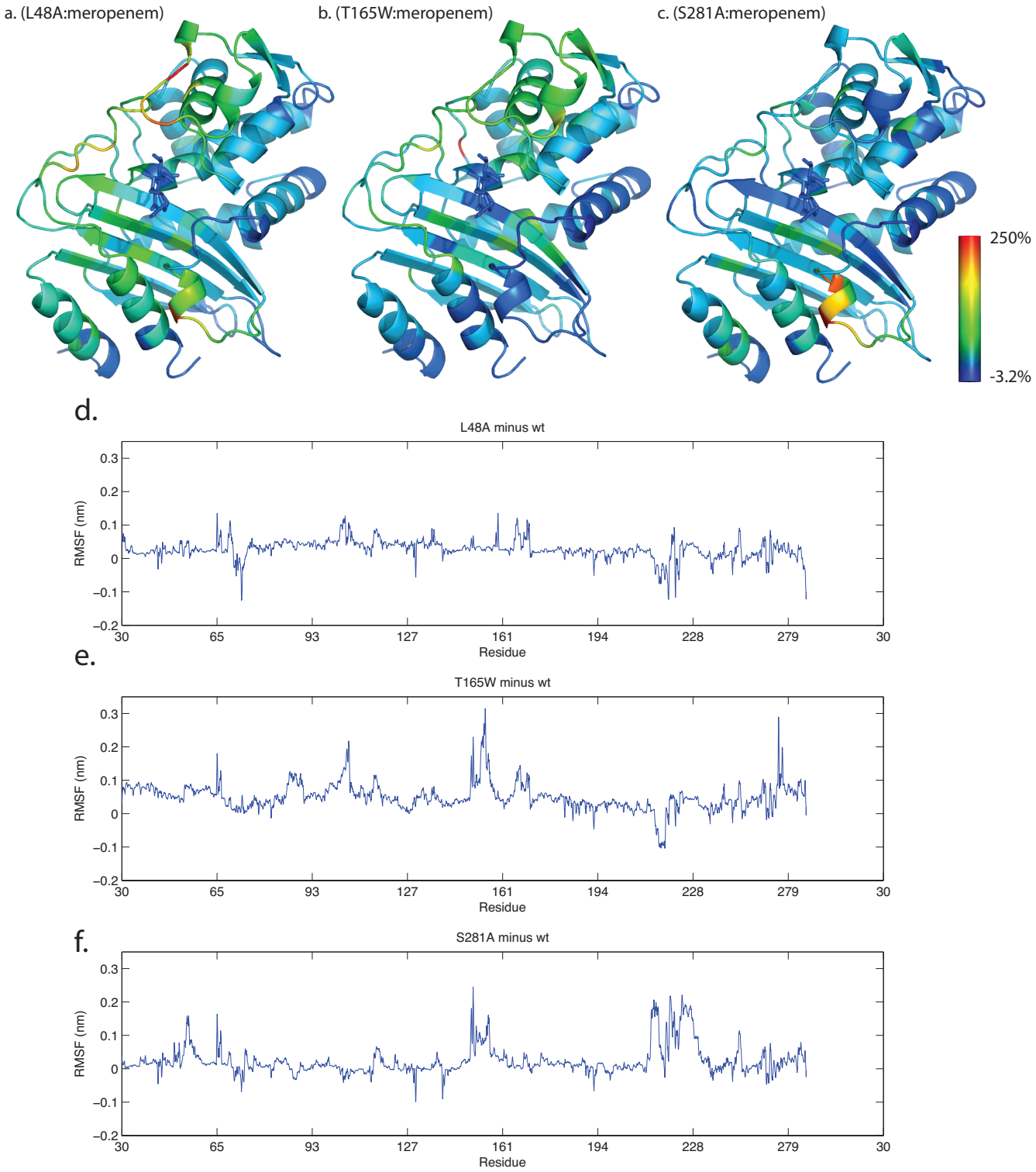

Figure S10. Residues of mutant enzymes showing increased flexibility compared to wild-type in simulations with meropenem. Each CTX-M9 mutant is rendered with residues colored from blue to red in order of increasing percent difference RMSF compared to the corresponding residue in simulations of wild-type CTX-M9. This yields a visual interpretation of which residues show increased conformational flexibility, which is quantitated as a set of per-residue RMSF plots in panels **d**-**f**.

Ranking	Residue / Atom	Mutual Information (meropenem)
1	234 / O	0.47
2	166 / CG	0.36
3	104 / O	0.28
4	166 / C	0.28
5	166 / CA	0.26
6	166 / CD	0.26
7	166 / CB	0.26
8	166 / O	0.26
9	166 / N	0.26
10	104 / C	0.26
Ranking	Residue / Atom	Mutual information (cefotaxime)
1	104 / ND2	0.51
2	104 / O	0.49
3	104 / CB	0.44
4	104 / CG	0.42
5	104 / OD1	0.40
6	105 / CD1	0.39
7	105 / CE1	0.36
8	105 / CD2	0.33
9	166 / CG	0.31
10	104 / C	0.31

Table S4. Ranking by positional mutual information of binding-pocket atoms that change position with allosteric mutations. Positional mutual information was used to rank binding-pocket atoms simulation snapshots from simulations of L48A, T165W, S281A, and CTX-M9 enzymes in acylenzyme complex with meropenem (top) and cefotaxime (bottom). The mutual information score $I(x, s)$ was computed between the aligned distance x of each atom from a CTX-M9 reference crystal structure (PDB 1YMX)[20] and the protein sequence s. The top 10 atoms by this feature-selection criterion are listed in ranked order. For simulations in complex with cefotaxime, 234/O is ranked 15th. We regard the meropenem mutual information rankings as more accurate because of better statistical sampling.

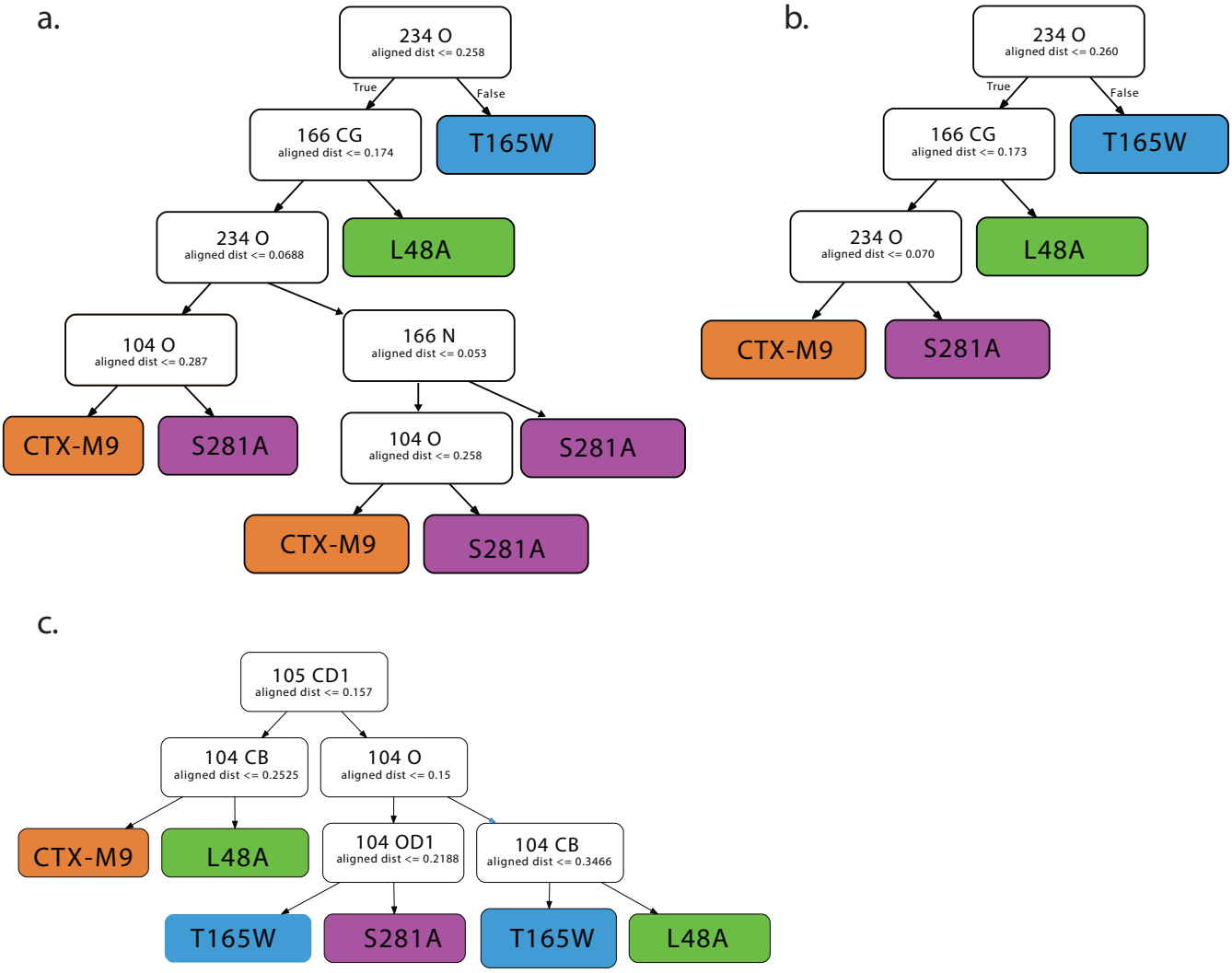

Figure S11. Binding-pocket atoms that shift position with allosteric mutations. Rendered is a decision tree trained on top-scoring binding-pocket atoms that uses the aligned distance in each simulation snapshot of each atom from a reference CTX-M9 wild-type crystal structure in complex with cefoxitin (PDB ID 1YMX)[20] to classify the mutant being simulated. Since this procedure is performed on binding-pocket atoms only, it identifies the binding pocket atoms most reflective of allosterically induced conformational changes. Binary decision trees were trained on acylenzyme simulations in complex with meropenem using the 10 top-scoring atoms and (1) unrestricted tree size, (2) tree size restricted to 7 leaf nodes (panel **a**), and (3) tree size restricted to 4 leaf nodes (panel **b**). These trees achieve a 10-fold cross-validation accuracy of 86.8 and test set classification accuracy of 86.9% for the 4-node tree, 89.3% cross-validation and 89.2% test set accuracy for the 7-node tree, and a cross-validation accuracy of 95.6% and a test set classification accuracy of 91% for the unrestricted tree. An unrestricted tree trained on all binding-pocket atoms (not just the top 10) achieved a cross-validation accuracy of 98.9% and a test-set accuracy of 97.9%. An additional decision tree trained on acylenzyme simulations in complex with cefotaxime is rendered in panel **c**. This had a cross-validation accuracy of 85.7% and test-set accuracy 85.5% when restricted to a maximum of 7 leaf nodes and 93.0% and 86% respectively when unrestricted in size but limited only to the top 10 binding-pocket atoms.

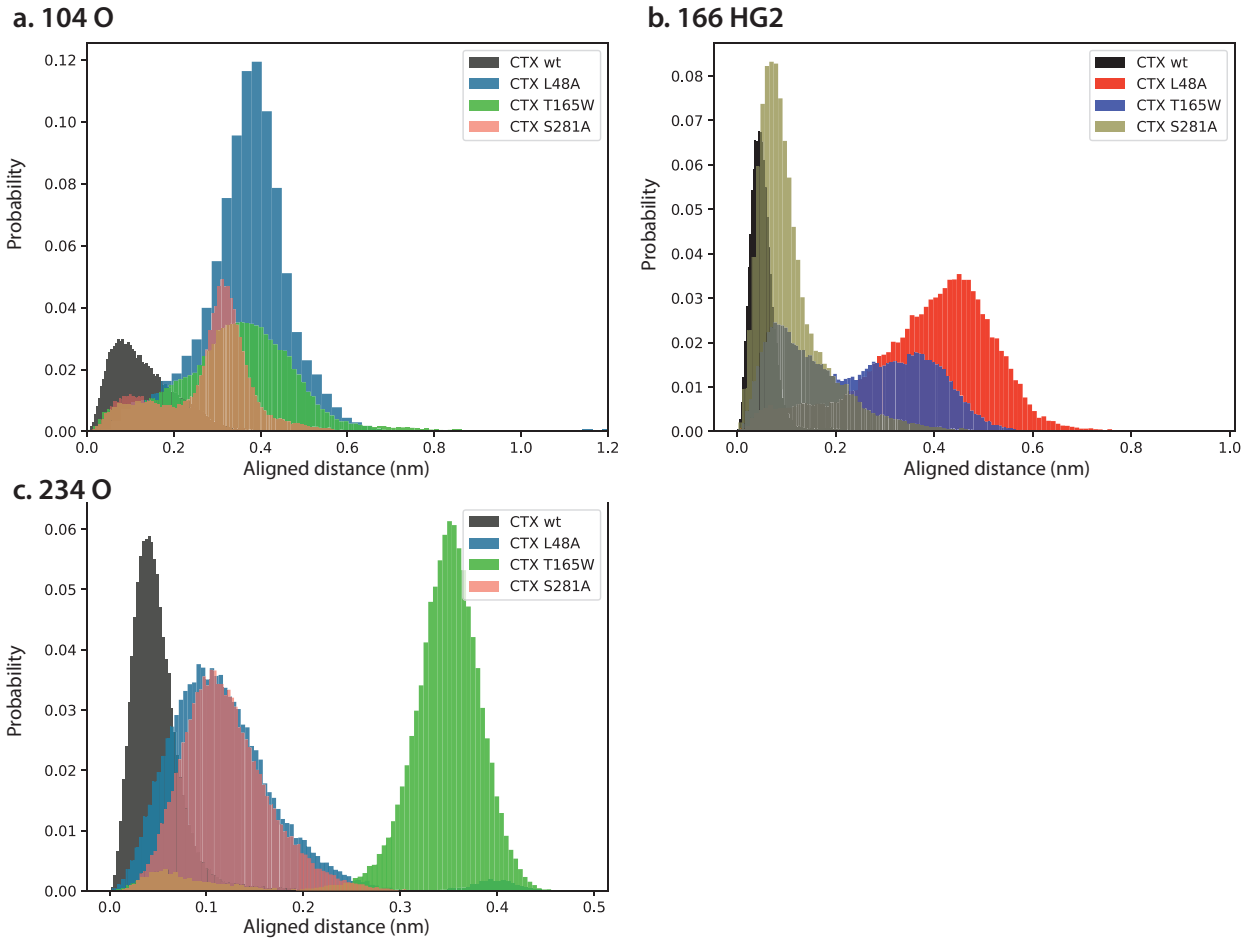

Figure S12. Displacement histograms for binding-pocket atoms that most shift position with allosteric mutations. Histograms of aligned distance from meropenem simulation with reference to each simulation start state are plotted for the three top-scoring binding-pocket atoms. All mutants have conformations in which the atoms are well-aligned with wild-type CTX-M9, but at least one mutant shows a substantial shift in the conformational distribution from wild-type for each top-scoring atom. Alternate colors in the histogram are used to help visualize this distributional overlap.

Residue	% Conservation in CTX-M	Variants	% Conservation across class A beta lactamases
48	99%	L, Q, V	12%
104	100%	N	39%
105	100%	Y	55%
165	99%	T, N	9%
166	99%	E, A	>99%
234	99%	K, R	>99%
281	75%	S, A, K	27%

Rank	Co-varies with L48	MI_p	Co-varies with T165	MI_p	Co-varies with S281	MI_p
1	220	0.27	140	0.26	288	0.21
2	82	0.22	72	0.21	39	0.20
3	225	0.21	135	0.20	273	0.15
4	279	0.19	147	0.17	230	0.14
5	254	0.17	96	0.16	105	0.13

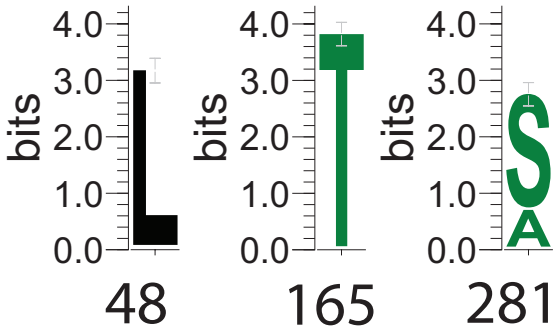

Table S5. Sequence conservation and co-variation of allosteric mutation sites. Tabulated above are sequence conservation of top-ranking allosteric mutation sites and binding-pocket residues that may transmit the effects of these allosteric mutations. Conservation was computed over a multiple-sequence alignment of the CTX-M beta lactamase family, with the dominant amino acid underlined and any other variants present in CTX-M listed. In all cases, CTX-M9 contains the dominant amino acid. Conserva-

tion was also computed across a multiple-sequence alignment of class A beta lactamases; the more distantly related class C and class D beta lactamases were not included because the catalytic residues (e.g. the identity of the general base) differ in these enzymes and thus although they have similar folds, the biochemistry at the active site is different[21, 22]. Class A beta lactamases share catalytic residues but differ in substrate specificity (and thus in substrate-positioning active site residues such as 104 and 105). Sequence co-variation was computed as phylogenetically corrected mutual information (MI_p)[15], and the top five residues linked to each of the three allosteric sites are listed. Sequence logos[23] are also listed for the top-ranking allosteric sites. Details on multiple sequence alignments and calculations are given in the Supplementary Methods.

Rank	**WT:cefotaxime**	**WT:meropenem**	**Mutant:cefotaxime**	**Mutant:meropenem**
Highest positional mutual information from residue 48				
1	70 / 6.4e-4	234 / 5.5e-4	234 / 3.4e-2	245 / 1.4e-2
2	130 / 5.8e-4	276 / 3.7e-4	245 / 3.3e-2	69 / 1.3e-2
3	73 / 5.6e-4	71 / 2.6e-4	235 / 2.3e-2	70 / 1.2e-2
4	131/ 5.4e-4	235 / 1.8e-4	238 / 1.2e-2	73 / 7.4e-3
5	234 / 5.2e-4	68 / 1.7e-4	236 / 1.1e-2	68 / 7.4e-3
Highest positional mutual information from residue 165				
1	166 / 1.9e-1	166 / 2.5e-1	166 / 2.0e-1	166 / 2.4e-1
2	169 / 5.3e-2	169 / 5.9e-2	169 / 1.4e-1	169 / 7.1e-2
3	170 / 3.6e-2	135 / 4.0e-2	170 / 5.2e-2	170 / 4.8e-2
4	70 / 3.1e-2	132 / 3.2e-2	69 / 1.4e02	104 / 2.0e-2
5	135 / 2.7e-2	170 / 3.1e-2	132 / 1.4e-2	105 / 2.0e-2
Highest positional mutual information from residue 281				
1	276 / 5.3e-2	276 / 9.8e-2	276 / 1.4e-1	276 / 7.7e-2
2	73 / 2.5e-2	234 / 4.2e-2	245 / 7.1e-2	135 / 1.4e-2
3	131 / 2.3e-2	69 / 3.0e-2	235 / 4.4e-3	131 / 1.3e-2
4	70 / 2.3e-2	68 / 2.2e-2	234 / 4.2e-2	126 / 1.3e-2
5	234 / 2.1e-2	71 / 2.1e-2	236 / 4.2e-2	245 / 1.1e-2

Table S6. Residue-residue positional mutual information between top allosteric mutant sites and the binding pocket. Positional mutual information (normalized to symmetric uncertainty) was calcu-

lated between each of the top three experimentally tested allosteric mutation sites and each binding-pocket residue over each of four simulation datasets. Residues were ranked by the top-scoring atom-atom symmetric uncertainty value for each residue pair, and the top five binding-pocket residues linked to each mutation site were tabulated along with their corresponding symmetric uncertainty value. Residues identified by the decision-tree analysis (Fig. S11) are shaded in gray.

Residue	% Rank via KINARI	% Rank via ProFlex
71	98	82
132	98	54
216	92	66
235	97	70
236	94	78
245	99	81
264	99	61

Table S7. Rigidity analysis identifies mutations more likely to disrupt CTX-M9 stability or function. As an alternate approach, we performed rigidity analyses of CTX-M9 using the KINARI[16] and MSU ProFlex[17] packages. Analytic details are given in the Supplementary Methods above. High-scoring residues are compared to seven previously reported[4] CTX-M9 alanine point mutants that de-creased drug resistance. The above table lists the percentile rank (with higher percentile being higher rank) of each of these alanine point mutants via each method. One previously reported mutant that is known to directly interact with the drug (R276A) was removed from comparison.

Supplemental References:

1. N. Collaborative Computational Project, *Acta Crystallogr D Biol Crystallogr*, 1994, **50**, 760-763.
2. A. J. McCoy, R. W. Grosse-Kunstleve, P. D. Adams, M. D. Winn, L. C. Storoni and R. J. Read, *J Appl Crystallogr*, 2007, **40**, 658-674.
3. P. Emsley, B. Lohkamp, W. G. Scott and K. Cowtan, *Acta Crystallogr D Biol Crystallogr*, 2010, **66**, 486-501.
4. G. A. Cortina and P. M. Kasson, *Bioinformatics*, 2016, **32**, 3420-3427.
5. Y. Chen, J. Delmas, J. Sirot, B. Shoichet and R. Bonnet, *J Mol Biol*, 2005, **348**, 349-362.
6. A. Fiser and A. Sali, *Methods Enzymol*, 2003, **374**, 461-491.
7. S. Pronk, S. Pall, R. Schulz, P. Larsson, P. Bjelkmar, R. Apostolov, M. R. Shirts, J. C. Smith, P. M. Kasson, D. van der Spoel, B. Hess and E. Lindahl, *Bioinformatics*, 2013, **29**, 845-854.
8. H. Li, A. D. Robertson and J. H. Jensen, *Proteins*, 2005, **61**, 704-721.
9. G. Bussi, D. Donadio and M. Parrinello, *J Chem Phys*, 2007, **126**, 014101.
10. T. Darden, D. York and L. Pedersen, *Journal of Chemical Physics*, 1993, **98**, 10089-10092.
11. B. Hess, *J. Chem. Theory Comput*, 2008, **4**, 116–122.
12. R. Canton, J. M. Gonzalez-Alba and J. C. Galan, *Front Microbiol*, 2012, **3**, 110.
13. R. D. Finn, J. Clements and S. R. Eddy, *Nucleic Acids Res*, 2011, **39**, W29-37.
14. R. C. Edgar, *Nucleic Acids Res*, 2004, **32**, 1792-1797.
15. S. D. Dunn, L. M. Wahl and G. B. Gloor, *Bioinformatics*, 2008, **24**, 333-340.

16. N. Fox, F. Jagodzinski, Y. Li and I. Streinu, *Nucleic Acids Res*, 2011, **39**, W177-183.
17. D. J. Jacobs, A. J. Rader, L. A. Kuhn and M. F. Thorpe, *Proteins*, 2001, **44**, 150-165.
18. S. G. Waley, *The Biochemical journal*, 1991, **279 (Pt 1)**, 87-94.
19. M. G. Page, *The Biochemical journal*, 1993, **295 (Pt 1)**, 295-304.
20. Y. Chen, B. Shoichet and R. Bonnet, *J Am Chem Soc*, 2005, **127**, 5423-5434.
21. A. Szarecka, K. R. Lesnock, C. A. Ramirez-Mondragon, H. B. Nicholas, Jr. and T. Wymore, *Protein Eng Des Sel*, 2011, **24**, 801-809.
22. Y. Chen, G. Minasov, T. A. Roth, F. Prati and B. K. Shoichet, *J Am Chem Soc*, 2006, **128**, 2970-2976.
23. G. E. Crooks, G. Hon, J. M. Chandonia and S. E. Brenner, *Genome Res*, 2004, **14**, 1188-1190.